

Chapter 7

Value of OLEDs with Field-Effect Electron Transport for Lasing Applications

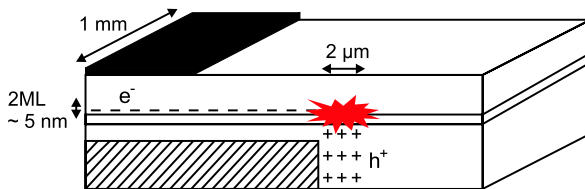
Organic light-emitting diodes (OLEDs) [84, 96, 215] and organic light-emitting field-effect transistors (LEOFETs) [49, 65, 75, 221, 222] are two device architectures that have been proposed as potential device configuration for future electrically pumped lasers. In this work, OLEDs with field-effect electron transport were added to the list of existing electroluminescent devices. The aim of the present chapter is to investigate the prospects of realizing an electrically pumped laser using these OLEDs with field-effect electron transport. First, the potential of the structure as laser device configuration is analyzed. The advantages as well as the existing limitations are highlighted. Next, amplified spontaneous emission measurements and optically pumped lasing experiments are performed. Stimulated emission in the host-guest system Alq₃:DCM₂ and in organic layer stacks including hole- and electron-transporting layers used in OLEDs with field-effect-assisted electron transport are studied. In the end, the different possibilities to incorporate an optical feedback mechanism in the device are discussed.

7.1 Potential of OLEDs with Field-Effect Electron Transport as Laser Device Configuration

OLEDs with field-effect electron transport exhibit several characteristics that are promising with respect to the realization of an electrically pumped organic laser. The high current density that can be achieved without significant reduction of the external quantum efficiency and the reduced optical absorption losses due to the remoteness of the metallic cathode, are the most important ones and are discussed in detail in Sect. 7.1.1 and Sect. 7.1.2, respectively.

Apart from minimizing the optical absorption losses and allowing high current densities, OLEDs with field-effect electron transport may also be able to reduce the triplet population in the device. In Chap. 5 (Sect. 5.1) it has been demonstrated that pulses as low as 1 μs could be applied to the device without affecting the light intensity. Since this pulse width is much shorter than the typical triplet lifetime of

Fig. 7.1 Illustration of the areas taken into account to calculate the electron and hole current density



fluorescent materials, pulsed excitation of the device may reduce triplet accumulation. In addition, since the electrons are transported by field-effect, high mobilities are achieved, reducing the number of charge carriers needed to generate population inversion in the device. The combination of all these properties makes OLEDs with field-effect electron transport interesting for waveguide devices and future electrically pumped lasers.

7.1.1 High Current Densities

In Chap. 3 and Chap. 4 it has been demonstrated that very high current densities can be achieved in OLEDs with field-effect electron transport without significant reduction of the external quantum efficiency. Using the electron-transporting material PTCDI-C₁₃H₂₇ a maximum electron and hole current density of, respectively, 5400 A/cm² and 13 A/cm² could be measured. The large difference between both values is due to the fact that for the calculation of the electron current density the thickness of the accumulation layer, which is about 5 nm [45, 256], was used, whereas for the hole current density the lateral area of the recombination zone ($\sim 2 \mu\text{m}$, Sect. 3.3) was taken into account. This is illustrated in Fig. 7.1.

The feasibility of electrically pumped lasing using OLEDs with field-effect electron transport can be investigated by calculating the exciton density per unit area in the recombination zone σ_{RZ} . This exciton density can be estimated using [69]:

$$\sigma_{RZ} = \frac{J}{q} \cdot r_{st} \phi_{PL} \tau, \quad (7.1)$$

where J is the current density, q is the elementary charge, r_{st} is the singlet/triplet ratio of excitons, ϕ_{PL} is the photoluminescence efficiency and τ is the exciton lifetime. For lasing it is the hole current density of 13 A/cm² that is most relevant because this takes into account the amount of excitons generated over the entire width of the recombination zone. The photoluminescence efficiency of DCM₂ was measured to be about 40% and is in agreement with previous reports [41]. The exciton lifetime of DCM₂ is 1 ns [333] and for fluorescent devices only a quarter of the injected charge carriers forms singlet excitons [36]. Using these values an exciton density of $8 \cdot 10^9 \text{ cm}^{-2}$ could be calculated. This value is lower than the typical values of exciton densities needed to reach the threshold in optically pumped lasers ($\sim 10^{11} - 10^{12} \text{ cm}^{-2}$ [69, 184, 221]), indicating that the achievable current density in OLEDs with field-effect electron transport is still insufficient to allow electrically pumped lasing.

The maximum achieved exciton density per unit area of our device concept is, however, still higher compared to other promising device architectures. Naber *et al.* reported a σ_{RZ} value of $1 \cdot 10^9 \text{ cm}^{-2}$ for polymer light-emitting field-effect transistors using a combination of a low- k and a high- k material as gate dielectric [69]. For the tetracene-based single crystal LEOFETs of Takenobu *et al.* they calculated $\sigma_{RZ} = 5 \cdot 10^6 \text{ cm}^{-2}$ [69]. Performing the same calculation for the LEOFET reported by Namdas *et al.* [63], using I (50 μA), W (1000 μm), W_{RZ} (4 μm), ϕ_{PL} (53% [221]) and τ (5 ns [221]) gives $\sigma_{RZ} = 5 \cdot 10^9 \text{ cm}^{-2}$. The slightly higher σ_{RZ} achievable in our devices is mainly attributed to the higher current densities that can be obtained and might be further improved by reducing the distance to the insulator edge, by using pulsed operation to higher voltages, by employing high- k dielectrics with low leakage current, by optimizing the device geometry and by using other light-emitting materials with a higher photoluminescence efficiency and/or a larger exciton lifetime. Note that the incorporation of triplet-emitters might also enhance σ_{RZ} since in this case $r_{st} = 100\%$, although other loss mechanisms such as triplet-triplet absorption and triplet-triplet annihilation may become dominant in that case (Sect. 6.2).

7.1.2 Reduced Absorption Losses

A main challenge to overcome with respect to the realization of electrically pumped lasing are the additional losses due to absorption of photons at the electrical contacts. In thin waveguide structures, where the resonator is positioned in the plane of the film, this is particularly important because of the long interaction between the light and the electrodes. OLEDs with field-effect electron transport may significantly reduce these detrimental waveguide losses, because the metallic cathode is displaced from the light-emitting zone.

Numerical simulations using the free full-vectorial Maxwell solver CAMFR¹ allowed us to compare the waveguide losses in OLEDs with field-effect electron transport to those in standard OLEDs. In CAMFR the materials are characterized by complex refractive indices. For the Al cathode and the ITO anode a value of, respectively, 1.040-6.189j and 1.823-0.003j was used. The imaginary part of the refractive index of the organic layer was assumed negligible. An organic layer with a thickness of 200 nm was taken for both device architectures. The results of the simulations are summarized in Table 7.1. Clearly, the OLED with field-effect electron transport shows a significant reduction of the optical absorption losses compared to conventional OLED structures, indicating that the absence of Al in the vicinity of the recombination zone indeed substantially decreases the waveguide losses. This reduction becomes more important at decreasing ITO thickness. When the devices comprise an anode of only 20 nm ITO, the waveguide losses are reduced by a factor ten.

¹Cavity Modelling FFramework (developed at INTEC, Ghent University, Belgium).

Table 7.1 Waveguide losses in conventional OLEDs and OLEDs with field-effect electron transport for various thicknesses of the ITO anode

	OLED	OLED with field-effect transport
ITO = 100 nm	256 cm^{-1}	104 cm^{-1}
ITO = 20 nm	222 cm^{-1}	21 cm^{-1}

The influence of the contact materials on the properties of the organic waveguide can also be experimentally analyzed by a combination of ASE and waveguide propagation loss measurements. For this purpose a series of multi-layer slab waveguide samples based on 150-nm thick MeLPPP films were prepared. MeLPPP was chosen because of its excellent film-forming properties, its high photoluminescence quantum efficiency in solid-state ($\sim 30\%$) and its large gain coefficient [157]. For each of the fabricated samples, the emission spectra for various excitation fluences were recorded. Plotting the emitted intensity at the peak wavelength ($\lambda = 495 \text{ nm}$) as a function of the excitation intensity allowed to determine the ASE thresholds, as displayed in Fig. 7.2.

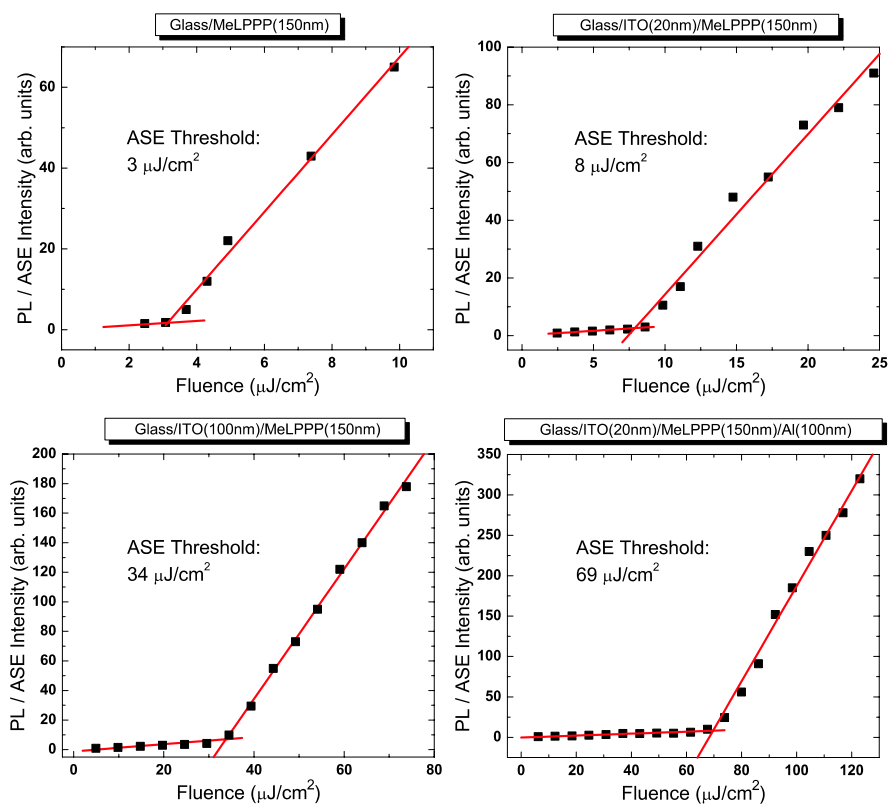


Fig. 7.2 ASE threshold measurements of different MeLPPP waveguide samples. (Measurements performed by RWTH Aachen)

The ASE threshold is determined as the excitation intensity at which the output signal slope efficiency abruptly increases. Clearly, the lowest ASE threshold of $3 \mu\text{J}/\text{cm}^2$ is achieved when MeLPPP is deposited on a bare glass substrate. A 20 and 100 nm thick ITO layer sandwiched between the organic film and the substrate results in an increase of the ASE threshold to, respectively, 8 and $34 \mu\text{J}/\text{cm}^2$. An additional Al layer on top of the organic waveguide further increases the ASE threshold to $69 \mu\text{J}/\text{cm}^2$. Note, that all samples were optically pumped from the back side, i.e. through the glass substrate. Therefore, strong absorption of the pump light by the metallic Al layer can be neglected when comparing the different samples.

One can expect that the observed increase in ASE threshold is based on a reduction of the optical confinement factor in the gain medium (reduced gain) and/or the extension of the waveguide modes into the absorbing contact layers (increased waveguide losses). Loss measurements, carried out by the experimental technique introduced in Chap. 2 (Sect. 2.2.5), allowed to determine the loss coefficient of the different waveguide structures. The results of these loss measurements, which actually provide information about the propagation of light in the unpumped region of the waveguides, are shown in Fig. 7.3. The graphs depict the edge emitted light intensity at $\lambda_{ASE} = 495 \text{ nm}$ as a function of the distance between the waveguide edge and the excitation stripe. For each sample the laser fluence was chosen above its respective ASE threshold. The data were fitted by an exponential decay function (solid lines) to extract the effective waveguide loss coefficients for the different layer stacks. Waveguide structures comprising absorbing layers adjacent to the MeLPPP organic layer show a significant increase in loss coefficients. The lowest waveguide losses of 5.3 cm^{-1} were observed for MeLPPP on a bare glass substrate. An additional ITO layer sandwiched between the organic film and the substrate increases the waveguide losses to 10.6 and 23.6 cm^{-1} for, respectively, 20 and 100 nm ITO thickness. The presence of an Al layer on top of the organic waveguide further increases the measured waveguide loss to the largest value of 47.6 cm^{-1} .

The first two columns of Table 7.2 summarize the measured ASE thresholds and waveguide losses of the investigated samples. As can be seen, higher ASE thresholds are accompanied by increased waveguide losses. The presence of Al has a large influence on these losses. Hence, OLEDs with field-effect electron transport, which have a metallic top contact displaced with respect to the recombination zone, will exhibit reduced optical absorption losses compared to conventional OLEDs, where light is generated very close to the metallic cathode. The measurements also show that the waveguide losses can be additionally reduced by decreasing the ITO layer thickness, which is in agreement with the simulated results obtained via CAMFR.

For a further evaluation of these results, the intensity profile of the light, which is propagating in the different structures, was simulated using a 2D beam propagation simulation tool (RSOFT BeamPROP). The optical constants of the involved materials were derived from ellipsometry measurements. The simulation results are displayed in Fig. 7.4. In each graph, the black line represents the vertical refractive index profile of the device structure. In lateral direction the sample is assumed to be infinite. Red lines represent the simulated vertical beam intensity profile within the structure. The amount of light guided within the active organic layer is marked by

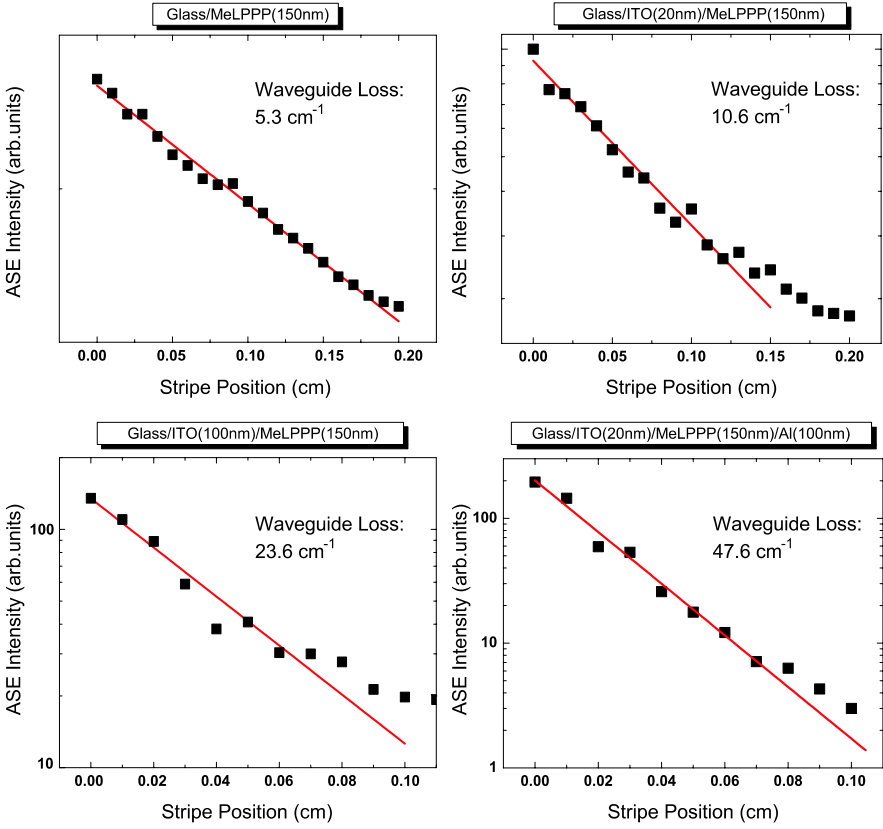


Fig. 7.3 Propagation loss measurements carried out for different MeLPPP waveguide samples. (Measurements performed by RWTH Aachen)

Table 7.2 ASE thresholds, loss coefficients and confinement factor of the investigated slab waveguide samples

sample	ASE threshold	loss coefficient	Γ
MeLPPP/glass	$3 \mu\text{J}/\text{cm}^2$	5.3 cm^{-1}	53%
MeLPPP/ITO(20 nm)/glass	$8 \mu\text{J}/\text{cm}^2$	10.6 cm^{-1}	50%
MeLPPP/ITO(100 nm)/glass	$34 \mu\text{J}/\text{cm}^2$	23.6 cm^{-1}	30%
Al/MeLPPP/ITO(20 nm)/glass	$69 \mu\text{J}/\text{cm}^2$	47.6 cm^{-1}	37%

the hatched area and the corresponding confinement factor Γ as well as the effective refractive indices n_{eff} of the whole structure are indicated. The confinement factors are summarized in the third column of Table 7.2.

The simulated data can be discussed with respect to their role on either lasing threshold or propagation losses. The losses of a certain structure are mainly de-

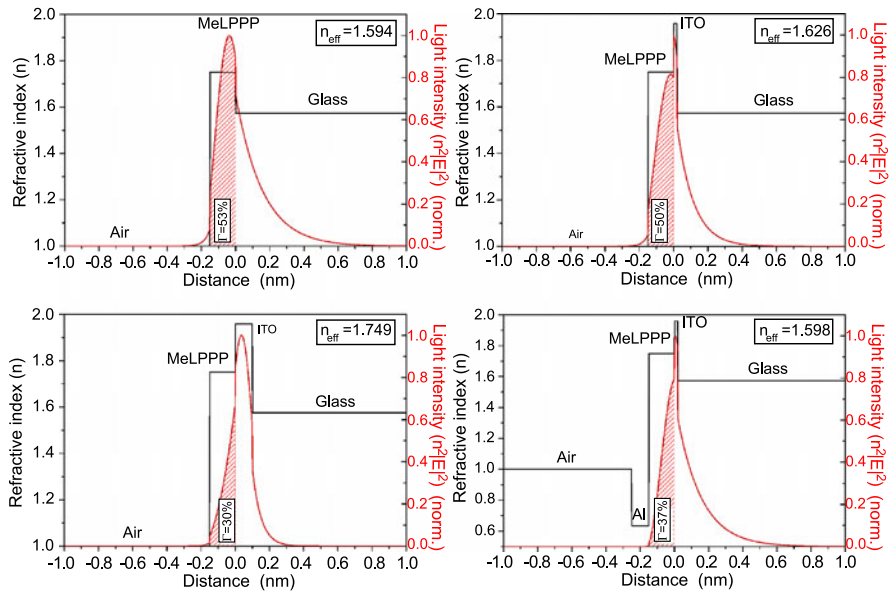


Fig. 7.4 (Color online) Simulated guided mode profiles for different MeLPPP waveguide samples. (Simulations performed by RWTH Aachen)

terminated by the percentage of light, which is guided within the lossy ITO and Al layers. For the ASE threshold, the amount of light guided within the active MeLPPP film (confinement factor) has to be taken into account additionally. A comparison between the different samples shows that the presence of 20 nm ITO only slightly decreases the confinement factor compared to the bare MeLPPP film. Consequently, the increase in ASE threshold from $3 \mu\text{J}/\text{cm}^2$ to $8 \mu\text{J}/\text{cm}^2$ for the former is mainly due to increased waveguide losses in this structure. When increasing the ITO thickness to 100 nm, the confinement factor drops from about 50% to 30%. In addition, the amount of light guided in the ITO layer and thus the accompanied waveguide losses strongly increase. Compared to the waveguide comprising a bare MeLPPP film, the ASE threshold increases by a factor of ten while the measured waveguide losses increase by only a factor of 4–5. This indicates that both the loss of confinement and the severe increase of waveguide losses are responsible for the order-of-magnitude increase in ASE threshold. Finally, the waveguide structure using Al has a confinement factor slightly better than the latter structure and the larger ASE threshold is clearly to be attributed to the waveguide losses provoked by the Al layer.

7.2 Optically Pumped Lasing Experiments

The active light-emitting layer of the OLEDs with field-effect electron transport presented in this work all consisted of an Alq₃ host matrix incorporating 2% of the

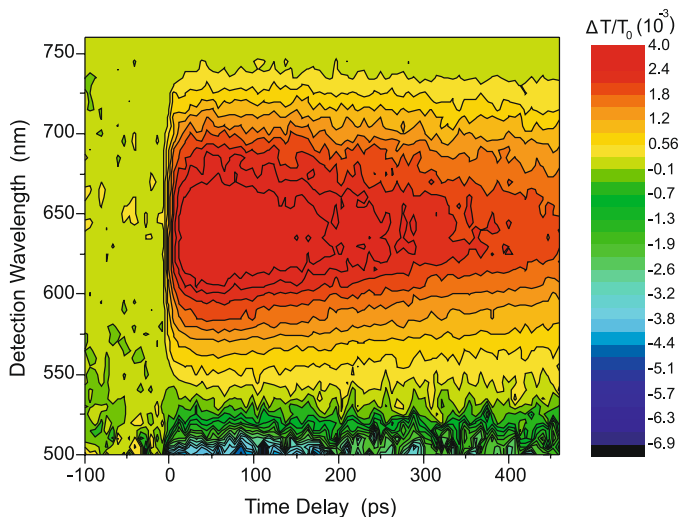


Fig. 7.5 Transient absorption measurement on a 150-nm thick $\text{Alq}_3\text{:DCM}_2$ layer, showing a maximum gain near 645 nm. (Measurements performed by RWTH Aachen)

red-emitting dye DCM_2 . $\text{Alq}_3\text{:DCM}_2$ is a benchmark host-guest system for which low ASE and lasing thresholds have been reported [114, 184]. In this section, stimulated emission of $\text{Alq}_3\text{:DCM}_2$ is investigated in single layers as well as in organic layer stacks including hole- and electron-transporting layers.

7.2.1 Stimulated Emission in $\text{Alq}_3\text{:DCM}_2$

To verify the wavelength with maximum gain of the host-guest system $\text{Alq}_3\text{:DCM}_2$ time-resolved pump-probe measurements have been performed on a 150-nm thick layer of Alq_3 doped with 2% DCM_2 , which was deposited on a quartz substrate. For these measurements, the excitation power was set to $110 \mu\text{J}/\text{cm}^2$. At this value ASE emission became well observable, but it was low enough to prevent sample degradation over the measurement's duration of 12 hours. The measured time-resolved transient absorption spectrum is presented in Fig. 7.5. Maximum gain is obtained at the spectral region around 640–650 nm. This gain region appears to be red-shifted compared to the photoluminescence spectrum which has its peak between 610–620 nm.

In a complimentary experiment, ASE has been observed in the same wavelength range. This is illustrated in Fig. 7.6, which shows the measured edge-emitted peak intensity of a 150 nm-thick $\text{Alq}_3\text{:DCM}_2$ film as a function of the pumping intensity. Above a pumping intensity of $6.6 \mu\text{J}/\text{cm}^2$, the slope efficiency of the output signal abruptly increases indicating that spontaneously emitted photons are exponentially amplified by stimulated emission. Since photons whose energy coincide with the spectral position of maximum gain will be amplified more than others, a collapse

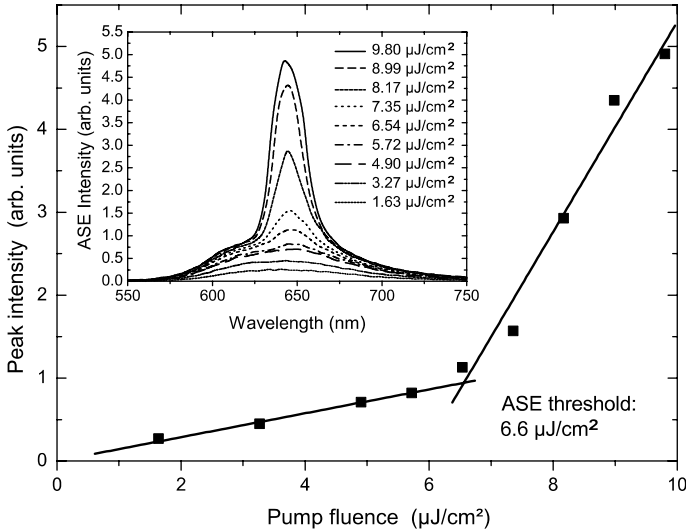


Fig. 7.6 Measurement of the edge emission as a function of the pump power. *Inset:* Evolution of the emission spectrum upon excitation density. Above the ASE threshold narrowing of the spectrum is observed. (Measurements performed by RWTH Aachen)

of the emission spectrum near 645 nm is observed. The evolution of the emission spectrum upon excitation density is shown as inset of Fig. 7.6.

Both measurements indicate that an optical feedback mechanism should be designed to have the resonator wavelength around 640–650 nm. While second-order photonic feedback structures are easier to characterize because of the vertical emission direction, first-order structures have a potentially lower lasing threshold because of the lack of vertical losses [146]. Hence, first-order linear grating structures were fabricated and used to perform optically pumped lasing experiments. Details about grating fabrication are discussed in Chap. 2 (Sect. 2.1.3). From photonic simulations the optimum photonic grating structure for the given technological and optical constraints was obtained. According to these simulations trenches of 50 nm depth were etched into SiO₂ with a period of 210 nm and a duty cycle of 50%. Figure 7.7 shows a SEM image of the cleaved cross section of the fabricated structure after organic layer deposition. Because the waviness of the grating is retained on the surface, an effective average thickness must be taken into account in the photonic simulations. Deposition of 200 nm organic material on top of the grating yields an effective thickness of 225 nm, which should result in the lowest threshold possible and a lasing wavelength between 640–645 nm.

Figure 7.8 shows the emission from 200 nm Alq₃:DCM₂ on the photonic grating structure. Lasing occurred at a wavelength of 639 nm, which is close to the optimum wavelength range between 640–645 nm. A lasing threshold of 110 pJ/pulse ($\sim 4 \mu\text{J}/\text{cm}^2$) and a slope efficiency of 0.0017 pJ^{-1} were extracted from the luminescence data. Because the grating was in first order and the lasing mode was guided in-plane, the sample had to be tilted with respect to the light collection lens by ap-

Fig. 7.7 SEM cross-section of the fabricated photonic structure covered with 200 nm $\text{Alq}_3:\text{DCM}_2$. (Image received from IBM Research Zurich)

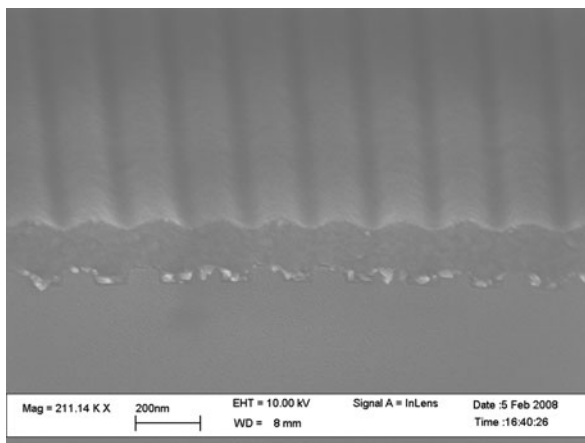
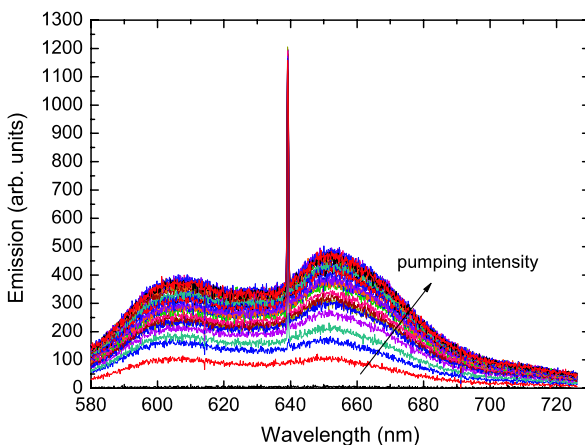


Fig. 7.8 Lasing emission from a first order photonic grating structure covered with 200 nm $\text{Alq}_3:\text{DCM}_2$. A lasing peak emerges from the photoluminescence spectrum above the pump power threshold. The measurements were performed at room temperature using a pump wavelength of 400 nm. (Measurements done by IBM Research Zurich)

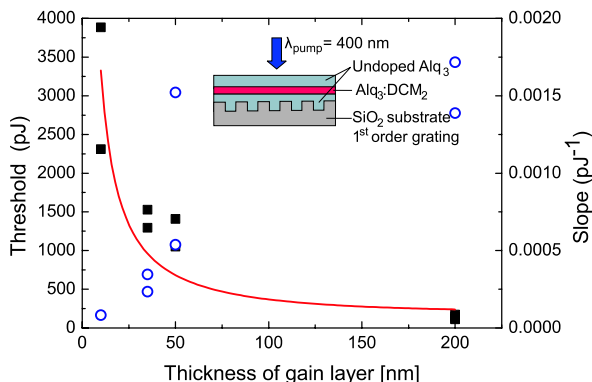


proximately 30° in order to be able to detect sufficient scattered light intensity. This tilting angle did not have a significant influence on the extracted values, but dramatically improved the signal-to-noise ratio. The presented lasing experiments were performed in close collaboration with IBM Research in Zurich.

7.2.2 Stimulated Emission in Stacks Comprising $\text{Alq}_3:\text{DCM}_2$

In OLEDs with field-effect electron transport the active light-emitting region has a thickness of about 20 nm. Such a thin gain layer implies a very low optical confinement factor in the vertical direction ($\Gamma \sim 4\%$), and currently it has not been shown that this can be successfully used to achieve optically pumped lasing in organic films. In order to assess this issue, a series of samples with Alq_3 layers on first order photonic gratings were fabricated in which the region doped with DCM_2

Fig. 7.9 Measured laser threshold (*squares*) and slope efficiency (*open circles*) as a function of thickness of gain layer. The *solid line* is the theoretical laser threshold expected from the calculated confinement factor. *Inset*: arrangement of the organic layer stack. (Measurements performed by IBM Research Zurich)



was systematically varied. The gain regions were always vertically centered in the layer stack in order to achieve good spatial overlap with the intensity maximum of the laser mode. This arrangement is illustrated in the inset of Fig. 7.9. The total thickness of the organic layer stack was 200 nm for all fabricated samples. The lasing behavior of this series of samples was investigated at room temperature using a femtosecond pulse laser having a pump wavelength of 400 nm.

Figure 7.9 displays the laser threshold and the slope efficiency as a function of thickness of the DCM₂-doped part. Lasing could be observed down to gain layer thicknesses of 10 nm. This is an interesting result since lasing for such thin organic gain layers has, to the best of our knowledge, never been demonstrated before. Compared to the device where the whole deposited organic layer shows gain, the laser threshold is, however, about one order of magnitude higher. This was expected from the calculated modal overlap. Accordingly, the slope efficiency of the laser decreases with decreasing gain layer thickness.

Next, the hole-transporting layer PTAA was included in the organic layer stack. 50 nm PTAA was spin-coated on top of a first order grating. Since the refractive indices of PTAA and Alq₃ match closely, the grating geometry could be retained. On top of the PTAA, varying thicknesses of DCM₂-doped Alq₃ were deposited, and the layer stack was completed to a total thickness of 200 nm by undoped Alq₃ as electron-transporting layer.

The luminescence spectra of a sample comprising 50 nm PTAA and 150 nm Alq₃:DCM₂, measured at various pumping intensities, are depicted in Fig. 7.10. Lasing was observed at 639 nm and a lasing threshold of ~ 400 pJ/pulse (~ 13 $\mu\text{J}/\text{cm}^2$) was measured. This threshold pump power is only slightly higher compared to the value achieved in absence of PTAA, which is an indication of good growth of Alq₃ on the spin-coated PTAA layer. The fact that the presence of PTAA does not change the laser threshold pump power significantly compared to Alq₃ is also noticeable from Fig. 7.11, which compares the laser threshold for a set of samples comprising different thicknesses of the DCM₂-doped layer on PTAA to the threshold values of Fig. 7.9. Both sets of data coincide nicely.

In the above mentioned organic layer stacks, Alq₃ was used as the electron-transporting layer. This material, however, cannot be used in OLEDs with field-

Fig. 7.10 Emission at room temperature from a lasing structure comprising a 50-nm thick PTAA hole-transporting layer on top of which 150 nm $\text{Alq}_3:\text{DCM}_2$ was deposited. Above the threshold a lasing peak appears in the spectrum. *Inset:* arrangement of the organic layer stack when comprising PTAA. (Measurements performed by IBM Research Zurich)

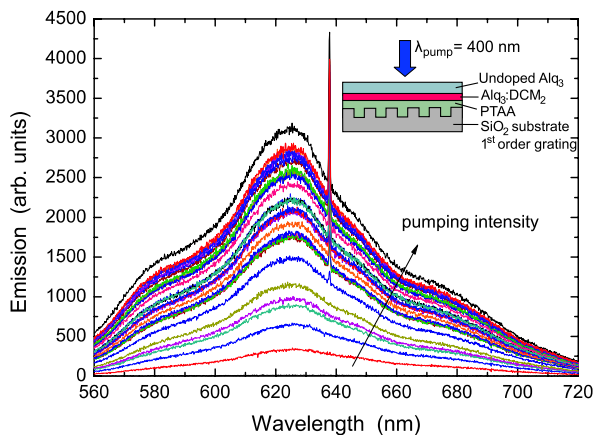
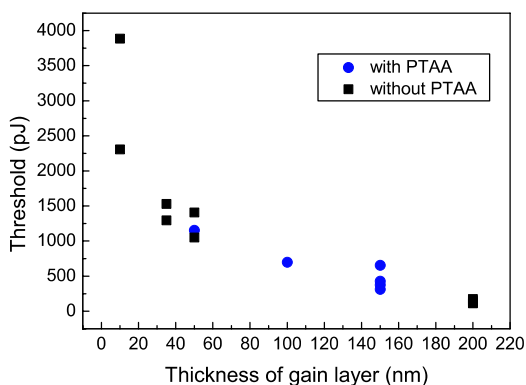


Fig. 7.11 Laser threshold values for a set of samples using different thicknesses of the DCM_2 -doped gain layer on top of PTAA (*circles*) measured at room temperature. An increase of the laser threshold is observed for thinner gain layers. The threshold for devices without PTAA have been shown for comparison (*squares*). (Measurements performed by IBM Research Zurich)



effect electron transport, because it does not conduct electrons in a thin-film transistor configuration (Sect. 3.2). Indeed, in OLEDs with field-effect electron transport, electrons are transported towards the light-emission zone by field-effect. This field-effect electron transport occurs in an electron accumulation layer formed at the hetero-interface with the active light-emitting layer $\text{Alq}_3:\text{DCM}_2$. The non-planar molecular structure of Alq_3 , however, prevents the formation of such an electron accumulation channel. Therefore, in order to optically pump organic layer stacks which are of direct use in OLEDs with field-effect electron transport, other electron-transporting materials have to be used. In this work, OLEDs with field-effect electron transport have been demonstrated using three different electron-transporting materials: PTCDI- $\text{C}_{13}\text{H}_{27}$, DFH-4T and DFHCO-4T. These three materials fulfil the two criteria that are important for device operation; they have a high electron field-effect mobility, and their LUMO is slightly lower than the LUMO of Alq_3 and DCM_2 , making electron transport possible at the heterojunction between the electron-transporting layer and the light-emitting layer. In addition, DFH-4T and DFHCO-4T exhibit a larger optical gap than PTCDI- $\text{C}_{13}\text{H}_{27}$, which results in lower absorption in the red spectral region.

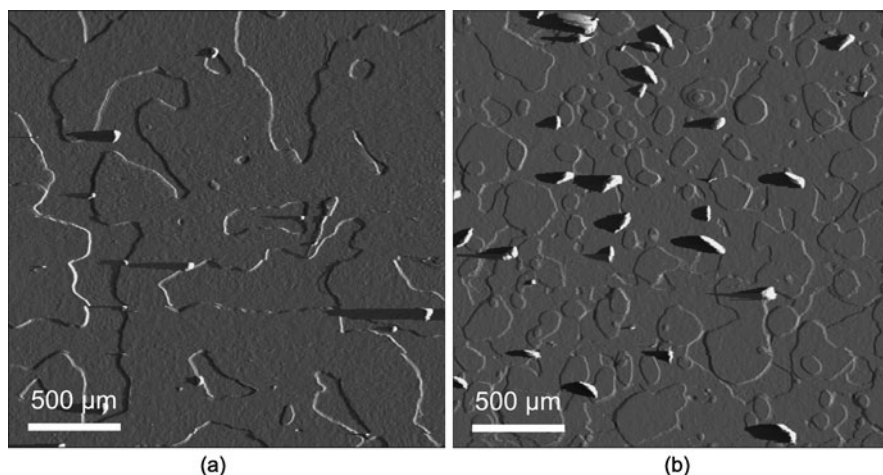


Fig. 7.12 $2.5\ \mu\text{m} \times 2.5\ \mu\text{m}$ AFM gradient image of (a) a 10-nm thick DFH-4T film deposited at $5\ \text{\AA}/\text{s}$, while the substrate was at 60°C , and (b) a 10-nm thick DFHCO-4T film deposited at $5\ \text{\AA}/\text{s}$ and a substrate temperature of 70°C

Because of this low absorption in the red spectral region, the losses under optical pumping are expected to be lower for samples comprising DFH-4T and DFHCO-4T compared to samples comprising PTCDI- $\text{C}_{13}\text{H}_{27}$. However, also other factors, such as surface roughness and film morphology of the electron-transporting material may influence the laser threshold. As discussed in Chap. 4 (Sect. 4.1), thin DFH-4T and DFHCO-4T films deposited by vacuum thermal evaporation show Stransky-Krastanov growth, implying that the growth of the first few monolayers is two-dimensional, but beyond a certain thickness threshold the film starts to roughen strongly (3D growth mode). This rough growth of DFH-4T and DFHCO-4T might be problematic for achieving lasing and has to be reduced as much as possible. Deposition at high substrate temperatures and high deposition flux largely suppressed the 3D growth (Sect. 4.1). A further reduction of the amount of 3D features was possible by reducing the organic layer thickness. Note that a minimum thickness of about 10 nm was necessary in order to form an electron accumulation layer for electron transport. Figure 7.12 shows the AFM gradient images of a 10-nm thick DFH-4T and a 10-nm thick DFHCO-4T film grown on top of P α MS under optimized growth conditions. The 3D needle growth is strongly suppressed. Only for the DFHCO-4T film a few 3D features could still be observed.

Different organic layer stacks were then deposited on top of first order photonic feedback structures. These stacks used 50 nm PTAA, followed by the deposition of 50 nm $\text{Alq}_3:\text{DCM}_2$ and the deposition of 10 nm of the electron-transporting material (PTCDI- $\text{C}_{13}\text{H}_{27}$, DFH-4T or DFHCO-4T). To obtain a total thickness of 200 nm, 90 nm undoped Alq_3 was evaporated on top of these structures. This arrangement is schematically illustrated in Fig. 7.13. In addition, a sample comprising 180 nm $\text{Alq}_3:\text{DCM}_2$ on top of a 20-nm thick ITO layer was fabricated. This ITO layer was sputtered on a first order grating structure before deposition of the organic layer. For

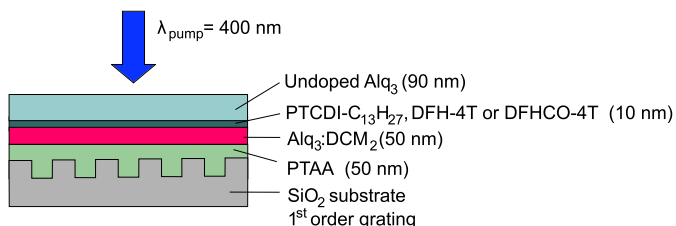


Fig. 7.13 Schematic illustration of the arrangement of the organic layer stack when comprising the electron-transporting layer PTCDI-C₁₃H₂₇, DFH-4T or DFHCO-4T

comparison, also an organic layer stack comprising 180 nm Alq₃:DCM₂ and 20 nm Alq₃ was fabricated.

Table 7.3 summarizes the measured average lasing thresholds of the different samples that were fabricated. For the structure comprising PTCDI-C₁₃H₂₇ as the electron-transporting material no lasing could be observed. This can be attributed to the substantial re-absorption of emitted photons by PTCDI-C₁₃H₂₇. The samples using DFH-4T and DFHCO-4T, on the other hand, did show lasing and an average lasing threshold of about 6000 pJ/pulse was measured for both structures. This observation is particularly encouraging because it indicates that optically pumped lasing can be achieved on material stacks including hole- and electron transporting layers which are of direct use in OLEDs with field-effect electron transport. The higher threshold of the DFH-4T and the DFHCO-4T samples compared to reference samples based on Alq₃ and with the same gain layer thickness is probably related to the layer morphology and the increased absorption at the pump wavelength ($\lambda = 400$ nm), since both materials should be transparent at the lasing wavelength ($\lambda \sim 640$ nm). Another interesting result is the fact that the presence of 20 nm ITO only slightly increased the lasing threshold. The lasing characteristics also were not modified due to the presence of ITO. This is in agreement with previous reports [182] and can be explained by the fact that 20 nm ITO introduces only very little absorption loss and does not significantly modify the confinement of the waveguide mode (Sect. 7.1.2).

From these measurements the exciton density at the laser threshold can be estimated. Taking into account a pump wavelength of 400 nm and a pump spot ra-

Table 7.3 Measured average lasing thresholds of different organic layer stacks deposited on first order gratings. Measurements were performed at room temperature using a pump wavelength of 400 nm

Sample	Average laser threshold
PTAA/Alq ₃ :DCM ₂ /PTCDI-C ₁₃ H ₂₇ /Alq ₃	–
PTAA/Alq ₃ :DCM ₂ /DFH-4T/Alq ₃	6188 pJ/pulse
PTAA/Alq ₃ :DCM ₂ /DFHCO-4T/Alq ₃	6122 pJ/pulse
ITO/Alq ₃ :DCM ₂	790 pJ/pulse
Alq ₃ /Alq ₃ :DCM ₂	490 pJ/pulse

dus on the sample of approximately 25 μm , a lasing threshold of ~ 6100 pJ/pulse corresponds to a photon density of $6 \cdot 10^{14} \text{ cm}^{-2}$ (or $300 \mu\text{J}/\text{cm}^2$) in the pump laser. Since the samples are optically pumped from the top, 35% of this incident energy is absorbed by the 90 nm thick undoped Alq₃ layer (Alq₃ absorption is $\alpha = 4.7 \cdot 10^4 \text{ cm}^{-1}$ at $\lambda = 400 \text{ nm}$) and 10% by the 10 nm thick electron-transporting layer ($\alpha_{DFHCO-AT} = 7.5 \cdot 10^4 \text{ cm}^{-1}$ at $\lambda = 400 \text{ nm}$). In addition, the Alq₃:DCM₂ gain layer absorbs only 20% of the energy at 400 nm excitation ($\alpha = 4.2 \cdot 10^4 \text{ cm}^{-1}$). This leads to an exciton density at the laser threshold of $\sim 7 \cdot 10^{13} \text{ cm}^{-2}$ for a device comprising an organic layer stack that is of direct use in an OLED with field-effect electron transport.

7.2.3 Discussion

As discussed in Sect. 7.1.1 the exciton density currently achieved under DC bias is estimated to be about $8 \cdot 10^9 \text{ cm}^{-2}$. To bridge the gap of several orders of magnitude, clearly, improvements will have to come from both sides, an increase in achievable σ_{RZ} and a decrease of required σ_{RZ} . The former was discussed in Sect. 7.1.1. For the latter, the strong sensitivity of the lasing threshold power to details of the structure (Table 7.3) indicates that order-of-magnitude improvements could be achieved by reducing residual absorption, by further optimizing waveguide losses, and by studying feedback structures with higher quality factor. This latter proposition will be further discussed in the next paragraph.

7.3 Device with Integrated Field-Effect and Photonic Features

There are different possibilities to incorporate a photonic feedback structure in an OLED with field-effect electron transport. Four possible resonator/device geometries are illustrated in Fig. 7.14. Figure 7.14(a) displays the situation where feedback is generated in the vertical direction, by placing distributed Bragg reflectors underneath and on top of the structure. In this case, feedback is perpendicular to the surface. Another option, which increases the gain length considerably, is to provide feedback in the lateral plane. Light is then waveguided in the organic film via internal total reflection. As suggested by Fig. 7.14(b–d) incorporation of a lateral feedback mechanism can be performed in different ways.

A very important figure of merit for lasing is the exciton density at the laser threshold N_{th} . The optical resonator has an influence on this parameter through two important factors: the optical confinement factor Γ and the quality factor Q of the laser cavity. N_{th} is inversely proportional to both Γ and Q :

$$N_{th} \sim \frac{1}{\Gamma Q} \quad (7.2)$$

Γ corresponds to the electric light field energy contained inside the region with optical gain normalized to the total energy, whereas Q is inversely proportional to

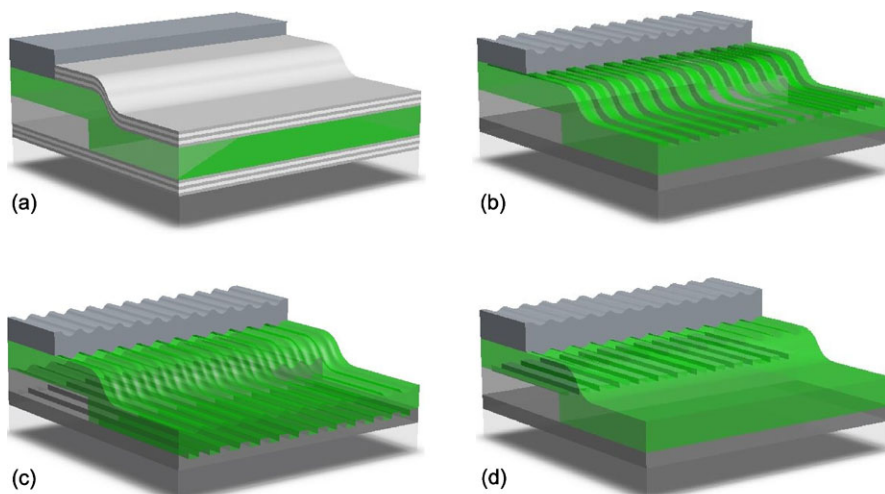


Fig. 7.14 Illustration of various possibilities to incorporate photonic feedback in an OLED with field-effect electron transport: (a) vertical resonator formed by DBR mirrors, (b) DFB structure imprinted in the organic layer stack, (c) DFB etched in the substrate before organic layer deposition, and (d) DFB structure etched in the insulator

the cavity loss coefficient and includes material absorption and output coupling from the resonator.

In close collaboration with IBM Research in Zurich, Γ and Q were calculated for, respectively, a vertically and a laterally oriented laser resonator structure, positioned around an organic layer stack comprising 120 nm PTAA, 20 nm $\text{Alq}_3\text{:DCM}_2$ and a 50-nm thick electron-transporting layer with low absorption losses such as DFH-4T or DFHCO-4T. The vertical resonator was formed by two DBR mirrors placed below and above the OLED with field-effect electron transport. Each of the 2×10 dielectric inorganic layer pairs were assumed to consist of 106 nm low refractive index material (SiO_2 , $n = 1.47$) and 74 nm high refractive index material (Ta_2O_5 ², $n = 2.15$). For the laterally oriented laser resonator, one-dimensional feedback was provided by extended SiO_2 ridges, having a width of 106 nm and a height of 100 nm.

Table 7.4 compares the Γ (in the vertical direction) and Q values calculated for both photonic feedback geometries. Due to the limited gain layer thickness the resulting confinement factors are quite small. This seriously increases the laser threshold of the device (Eq. (7.2)), however, as demonstrated in Sect. 7.2.2 such thin gain layers do not exclude lasing. Note that Quantum-Well III-V lasers have similar confinement factors [334, 335]. The quality factor of both resonator geometries is also given in Table 7.4. For the vertical geometry the Q factor is the result of the normal cavity losses formed by 10 DBR layer pairs for output coupling. The nature of the first order feedback in the lateral direction, on the other hand, allows a nearly perfectly guided mode without output coupling and correspondingly a high Q factor

²Tantalum pentoxide.

Table 7.4 Comparison of the Γ and Q values of a vertical and lateral resonator geometry

	vertical resonator	lateral resonator
Confinement factor Γ (%)	5.3	3.8
Quality factor Q	2862	17071
Q with ITO	1190	702
Q with ITO and strong-absorbing ETL	78	203

is calculated. To assess the impact of the presence of ITO on the Q factor, similar calculations were performed assuming the organic layer stack is positioned on top of a 100 nm thick ITO layer. For the lateral feedback configuration this results in a dramatic reduction of the Q factor, while the vertical resonator geometry does not suffer as much. In contrast, the Q factor of the vertical resonator decreases more when a strong-absorbing electron-transporting layer such as PTCDI-C₁₃H₂₇ is used. Clearly, these results suggest that the incorporation of a lateral feedback mechanism in OLEDs with field-effect electron transport comprising low-absorbing materials such as DFH-4T or DFHCO-4T as the organic electron-transporting material and using only a very thin ITO layer as the bottom electrode might be a promising route to follow.

7.4 Summary and Conclusions

In this chapter, the prospects of realizing an electrically pumped laser using OLEDs with field-effect electron transport were investigated. By numerical simulations as well as by experiments it was demonstrated that OLEDs with field-effect electron transport allow a substantial reduction of the absorption losses thanks to the remoteness of the metallic cathode. In addition, very high current densities in the order of 13 A/cm² were measured without significant reduction of the external quantum efficiency. Based on these high current densities an exciton density per unit area of $8 \cdot 10^9$ cm⁻² was calculated. Although this value is still several orders of magnitude lower than the values for the exciton density obtained from the threshold of optically pumped lasers, it is among the highest exciton densities per unit area reported to date for electrically pumped devices.

Amplified spontaneous emission measurements and optically pumped lasing experiments were performed on the host-guest system Alq₃:DCM₂ and on organic layer stacks including hole- and electron-transporting layers used in OLEDs with field-effect-assisted electron transport. Lasing could be achieved for gain layers of only 10 nm thick. However, the laser threshold was seriously increased for these thinner gain layers, which is in agreement with numerical simulations. It was found that the presence of the hole-transporting material PTAA does not change the laser threshold pump power significantly. Upon inserting electron-transporting materials, on the other hand, the laser threshold was increased about one order of magnitude. A thin layer of 20 nm ITO only slightly influenced the laser threshold. In the end, the

different possibilities to incorporate a photonic feedback structure in OLEDs with field-effect electron transport were discussed. The incorporation of a lateral photonic feedback configuration in combination with the use of low absorbing electron-transporting materials and a thin ITO anode, might be a promising route towards the realization of an electrically pumped organic laser.